Ocean Engineering 328 (2025) 121049

Contents lists available at ScienceDirect

Ocean Engineering

journal homepage: www.elsevier.com/locate/oceaneng

Research paper

Monolithic 3D numerical modeling of granular cargo movement on bulk carriers in waves

W. Düsterhöft-Wriggers*, T. Rung

Hamburg University of Technology, Am Schwarzenberg-Campus 1, Hamburg, 21073, Hamburg, Germany

ARTICLE INFO

Keywords:
Cargo liquefaction
Granular cargo
3DoF rigid body motion
Three-phase flow
Bulk carrier

ABSTRACT

A novel monolithic approach for simulating vessels in waves with granular cargo is presented using a Finite Volume framework. The integrated approach aims to develop a tool for maritime safety analysis and design optimization of bulk carriers. The computational model integrates a three-phase Volume of Fluid method to represent air, water, and cargo, coupled with a material model that applies a rigid-perfectly plastic material model for the granular phase. The approach takes into account the floating motion of the ship using a rigid body motion solver for three degrees of freedom and is supplemented by inviscid far-field boundary conditions facilitating the generation of linear waves approaching the vessel. The model's efficacy is demonstrated through a validation of the three-phase Volume of the Fluid method, a verification of the granular material model, and finally, a reconstruction of the accident of the "Jian Fu Star" bulk carrier in a fully 3D simulation.

1. Introduction

This paper introduces a fully coupled 3D three-phase model for cargo vessels transporting granular material in waves. Results of two validation and verification cases assessing the individual dynamics of the coupled model are presented, as well as a complete 3D case application study that recreate a vessel sinking incident. The reason for this study is the accumulative accidents involving bulk carriers transporting unsaturated ores between 2009 and 2019, which are summarized in Table 1 and claimed numerous fatalities. Other ships carrying nickel or iron ore had to abandon their voyage and/or take stability-enhancing measures to avoid capsizing. One of these incidents is described as an example in Lee (2017), and a general description of the problems of transporting nickel and iron ore on vessels can be found in Rose (2014) and Munro and Mohajerani (2016). Also, some historical accidents, such as the sinking of the vessel "Melanie Schulte" in 1952 (cf. Teutsch and Groll, n.d.), could be related to cargo instability, which is investigated in this work.

The effect that was blamed for the numerous losses of bulk carriers is called liquefaction and is a sudden viscous behavior of the loaded unsaturated granular material. Geotechnical liquefaction occurs when the forces resulting from pore pressure exceed the inter-particle forces and is mainly described in the context of earthquakes, e.g., Bian and Shahrour (2009), Di and Sato (2004a,b), Elgamal et al. (2002) and Unno et al. (2008). The liquefaction of unsaturated granular material is a challenging mechanism to simulate as seen in Wobbes et al. (2017) and Airey and Ghorbani (2021). Promising research, including the fluidization of granular material by pore gas pressure in the Finite Volume method, can be found in Chupin and Dubois (2024). Current research by Hoang et al. (2024a,b) applying Lagrangian Smoothed Particle Hydrodynamics (SPH) methods to solve geomechanical problems could be extended for application of bulk cargo transport provided that the coupled ship movement in the sea state is also simulated.

Based on the existing data from accidents and incidents, the causally responsible cargo failure mechanism needs to be identified. In addition to geotechnical liquefaction, cargo shifting and the so-called "wet base" or "dynamic separation" mechanisms can lead to stability problems of ships, cf. TWG Iron Ore Technical Working Group (2013), Rose (2014) and Ferauge et al. (2019). A "wet base" occurs if the water inside the cargo migrates towards the bottom so that a fully saturated layer of cargo forms at the bottom of the cargo hold. The ship's movement causes the highly saturated bottom layer to move and the more stable, drier upper part of the cargo to slide back and forth on the wet bottom layer.

The theory of "dynamic separation" is explained in Ferauge et al. (2019). It assumes that a highly saturated cargo layer forms on the upper cargo pile either due to compression of the cargo, which pumps the internal water upwards, or due to external water entering the ship. Captains' reports indicate that on ships where unstable cargo required emergency measures, water was found on top of the cargo piles and in the corners of the holds. Moreover, even pure sliding of the iron and nickel ore cargo can be the reason for the incidences, since the material's cohesion and angle of repose depend on the degree of saturation of the cargo material. Most lost vessels are reported to have left from

* Corresponding author.
E-mail address: wibke.wriggers@tuhh.de (W. Düsterhöft-Wriggers).

https://doi.org/10.1016/j.oceaneng.2025.121049
Received 1 January 2025; Received in revised form 20 March 2025; Accepted 20 March 2025
Available online 31 March 2025

Table 1
List of bulk carriers carrying nickel or iron ore lost due to cargo shift/ liquefaction from 2009 until 2024 as reported in the "Bulk Carrier Casualty Reports" of INTERCARGO (2019, 2021).

Vessel name	*LoA* [m]	*B* [m]	Year	Cargo	Loss of lives
Black Rose	187.7	28.4	2009	Indian iron ore fines	1
Asian Forest	128.0	20.0	2009	Indian iron ore fines	0
Jian Fu Star	189.8	31.3	2010	Indonesian nickel ore	13
Nasco Diamond	185.6	32.3	2010	Indonesian nickel ore	22
Hong Wei	189.8	32.3	2010	Indonesian nickel ore	10
Vinalines Queen	190.0	32.3	2011	Indonesian nickel ore	22
Harita Bauxite	192.0	32.0	2013	Indonesian nickel ore	15
Trans Summer	190.0	32.0	2013	Indonesian nickel ore	0
Bulk Jupiter	190.0	32.3	2015	Malaysian Bauxite	18
Emerald Star	190.0	32.0	2017	Indonesian nickel ore	10
Nur Allya	190.0	32.0	2019	Indonesian nickel ore	27

ports in regions where the monsoon rain was drenching the cargo before the vessel left. Such cargo sliding can also occur in dry bulk cargos, e.g., wood or grains, and the suggested method can therefore also be applied to incidents related to these cargoes, e.g., the incident of the "Yong Feng" in 2021.

The present approach does not assume geotechnical liquefaction but uses a classical perfectly plastic material model described in Düsterhöft-Wriggers et al. (2024), which depends on the cohesion and angle of repose of the material to represent the cargo behavior. A saturation-dependent cohesion and angle of repose are included in the employed model. By applying material parameters based on the information in the incident reports, this approach can represent the shifting of cargo during the incidents.

Other numerical models have been developed to study the cargo behavior on bulk carriers, some of which are similar to the approach of the present model. In Zou et al. (2013), a level-set-based Finite Volume (FV) free-surface method is used to study the sloshing of highly viscous fluids in rectangular tanks, missing a material model representing the granular phase. A Discrete Element Method (DEM) based model for simulating liquefaction on vessels has been developed by Ju et al. (2018, 2019). This approach provides a granular-level analysis of cargo behavior under maritime conditions. In a related study, Zhang et al. (2019) employed a coupled non-Newtonian fluid model with a simplified body surface method to investigate vessel responses. Their research examined the relationships between wave frequencies, amplitudes, and resulting ship motions. Wang et al. (2022) applied the DEM methods to explore the influence of material parameters on cargo movement. This study highlighted the critical role of specific cargo properties in determining the risk and extent of potential shifts during transit. Complementing these efforts, Wu et al. (2022) conducted a comprehensive analysis of liquefaction risk utilizing advanced 3D vessel simulations. These studies demonstrate the increasing complexity of computational models in addressing the challenges of maritime cargo transportation. In the present work, these studies are extended by a complete 3D model of a vessel with granular cargo in a seaway, which is derived from an incident report.

The paper is structured as follows: the mathematical model and numerical method are described in Sections 2 and 3. The validation of the three-phase and granular models is presented in Sections 4, and 5 is devoted to the results of a 3D case study of the coupled problem. The latter refers to the "Jian Fu Star" incident on 27th October 2010, cf. Table 1. The associated incident conditions are taken from the incident report of the "Panama Maritime Authority" (Investigation Department, 2011).

Within the publication, the Einstein summation convention is used for lower-case Latin subscripts. All vectors and tensors are defined with reference to Cartesian coordinates.

2. Mathematical model

The present approach solves the multi-physics problem of loading granular cargo on a vessel in seaway conditions monolithically. In addition to solving the momentum and continuity equations for a three-phase flow, cf. Luo and Rung (2019), a displacement equation is introduced to depict the cargo shift, cf. Section 2.1. The description of the cargo behavior employs a viscous material model to describe the granular cargo phase as an incompressible, perfectly plastic material. The vessel is modeled as a rigid body moving in three degrees of freedom in a seaways, cf. Section 2.2 and the wave field is generated by appropriate far-field boundary conditions Luo and Rung (2019, 2017), cf.

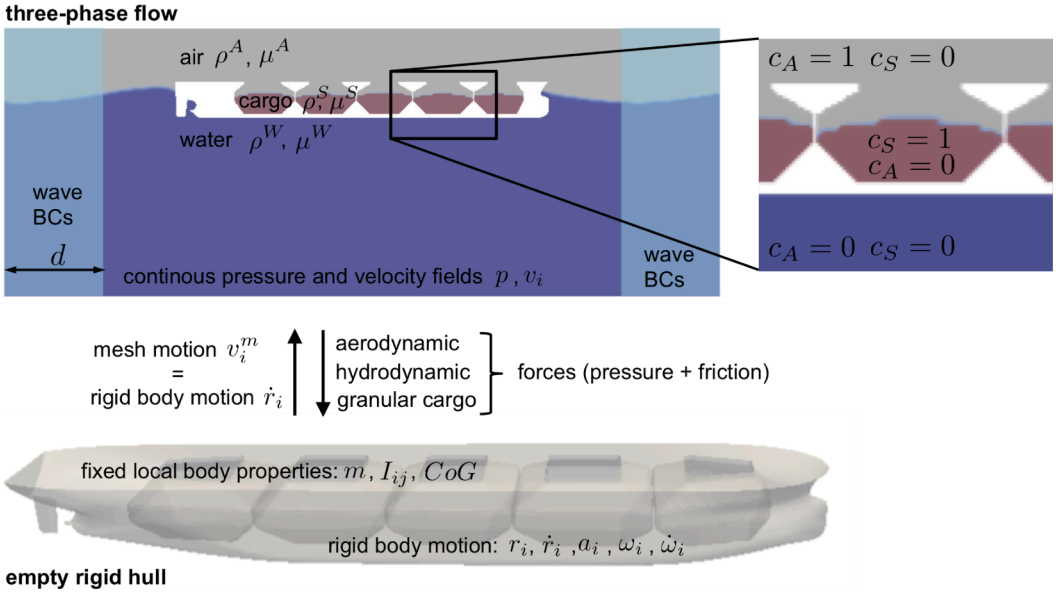

Fig. 1. Schematic of coupling between three-phase flow, rigid body motion and wave boundary conditions.

Section 2.3. Fig. 1 shows the interaction of the different modules of the procedure as well as the associated parameters and field variables.

2.1. Governing equations

The governing equations follow a fluid dynamic concept and consist of the Eulerian momentum and continuity equations, which are supplemented by an Eulerian displacement equation for the granular material. The three materials involved, air, water and granular material, are all associated with an incompressible (fluid) phase. As is usual in incompressible computational fluid dynamics, the equations are based on the velocities and pressure as dependent variables in an Eulerian framework.

The governing equations utilize algebraic equations of state to identify the local material properties from the local volume concentrations of the three involved material phases. The volume concentrations are determined from simple transport equations for immiscible phases using a Volume of Fluid (VoF) concept, cf. Hirt and Nicholls (1981).

2.1.1. Three-phase model

A three-phase VoF approach is employed to model the granular cargo motion inside a free-floating vessel in waves. To this end, local subvolumes V^A, V^S, V^W of a control volume $V = V^A + V^G + V^W$ and related volume fractions are introduced for the air, granular soil and water phase, i.e., $c_A = V^A/V$, $c_S = V^S/V$ and $c_W = V^W/V$.

Two simple mixture fraction transport equations for the air and soil fractions are employed, which represent their immiscibility. Assuming that the air and soil phases are immiscible, the Lagrangian condition $Dc_S/Dt = Dc_A/Dt = 0$ has to be fulfilled. The corresponding Eulerian equations read

$$\frac{\partial c_S}{\partial t} + \frac{\partial (c_S v_i)}{\partial x_i} = 0 \quad \text{and} \quad \frac{\partial c_A}{\partial t} + \frac{\partial (c_A v_i)}{\partial x_i} = 0, \tag{1}$$

where v_i is the local velocity, whose divergence vanishes for incompressible media due to continuity reasons. The mixture fraction of water follows from a compatibility relation $V = V_A + V_S + V_W$, viz.

$$c_W = 1 - c_A - c_S. \tag{2}$$

Having computed the mixture fractions, the local density ρ and viscosity μ of the mixture is given by

$$\rho = c_A \rho^A + c_S \rho^S + (1 - c_A - c_S)\rho^W, \tag{3a}$$

$$\mu = c_A \mu^A + c_S \mu^S + (1 - c_A - c_S)\mu^W, \tag{3b}$$

where the bulk properties are denoted by $(\dots)^A$ for the air phase, $(\dots)^S$ for the granular soil phase and $(\dots)^W$ for the water phase.

The present procedure refers to a cell-centered FV method and requires the reconstruction of cell-face properties from cell-centered values. When using a linear interpolation method for the interpolation of the granular material properties, creeping can occur at the top of the granular material. A nonlinear interpolation method based on an arctangent function given in Section 3.5 is used to interpolate granular material properties.

2.1.2. Material model for granular phase

The material model described in Eq. (3) requires the bulk properties of the three material phases. The bulk densities of all three are generally given. For laminar flows, the viscosity of the air and water phase refers to a constant value. For turbulent flows, μ^S and μ^A follow from an eddy-viscosity turbulence model (Wilcox, 2004). The bulk density of the granular soil phase μ^S is dynamically modeled from the local strain rate. As described in Düsterhöft-Wriggers et al. (2024), the material model for the granular phase is based on the Drucker–Prager yield criterion for perfectly plastic materials, which yields $\mu_S = (3\alpha_\phi p + k_c)/\sqrt{2\dot{\epsilon}_{ij}\dot{\epsilon}_{ij}}$. To increase the numerical robustness, the soil viscosity μ^S follows from a more continuous, regularized Bingham model

$$\mu^S = \mu^S_{\min} + \frac{3\alpha_\phi p + k_c}{\sqrt{2\dot{\epsilon}_{ij}\dot{\epsilon}_{ij}}} \left(1 - e^{-m\sqrt{2\dot{\epsilon}_{ij}\dot{\epsilon}_{ij}}}\right), \tag{4}$$

where $\dot{\epsilon}_{ij}$ is the (traceless) strain-rate tensor and p is the pressure. The material constants k_c and α_ϕ relate to simply measurable material properties,

$$\alpha_\phi = \frac{\tan\phi}{\sqrt{9 + 12\tan^2\phi}} \quad \text{and} \quad k_c = \frac{3C}{\sqrt{9 + 12\tan^2\phi}} \tag{5}$$

where C denotes the cohesion and ϕ the angle of repose of the granular material, cf., for example, Bui et al. (2008). The minimum viscosity is required to be as low as possible to match the assumed perfectly plastic behavior. It is assigned to a value of $\mu^S_{\min} = 10^{-3}$ [Pa s] in the current study, which agrees with the values communicated in Düsterhöft-Wriggers et al. (2024). The constant m determines the maximum viscosity, i.e. $\lim_{\dot{\epsilon}_{ij}\to 0} \mu^S = m(3\alpha_\phi p + k_c)$. The maximum viscosity is usually assigned a very high value to avoid creeping of the granular cargo, which leads to $m = 100$ in the current study.

2.1.3. Momentum and continuity equations

Using the immiscibility conditions $Dc_A/Dt = 0$, $Dc_S/Dt = 0$ as well as assuming incompressible bulk densities ρ^A, ρ^S, ρ^W, the continuity equation of the three-phase mixture can be simplified to the usual zero velocity-divergence condition

$$\frac{D\rho}{Dt} + \rho\frac{\partial v_i}{\partial x_i} = (\rho^A - \rho^W)\frac{Dc_A}{Dt} + (\rho^S - \rho^W)\frac{Dc_S}{Dt} + \rho\frac{\partial v_i}{\partial x_i} = 0 \;\rightarrow\; \frac{\partial v_i}{\partial x_i} = 0. \tag{6}$$

The momentum equations for the three-phase mixture reads

$$\frac{\partial(\rho v_i)}{\partial t} + \frac{\partial(\rho v_i v_j)}{\partial x_j} = \frac{\partial}{\partial x_j}\left[-p\delta_{ij} + \mu\left(\frac{\partial v_i}{\partial x_j} + \frac{\partial v_j}{\partial x_i}\right)\right] + \rho g_i \tag{7}$$

where μ, ρ are closed by the material model (3).

2.1.4. Cargo displacement

An Eulerian displacement equation is employed to represent the cargo's displacement. The cargo displacement is only needed for post-processing purposes and comparisons with classical Lagrangian approaches. The Eulerian displacement u_i is simply calculated from the material derivative

$$\frac{Du_i}{Dt} = v_i^S. \tag{8}$$

The velocity of the granular material v_i^S is obtained by multiplying the velocity field with the soil mixture fraction, i.e., $v_i^S = c^S v_i$, viz.

$$\frac{\partial u_i}{\partial t} + \frac{\partial(c_S v_j u_i)}{\partial x_j} = c_S v_i. \tag{9}$$

2.2. Rigid body motion

A rigid body motion is assumed for the vessel, neglecting possible structural deformations. To this end, a six degrees of freedom motion solver based on quaternions is coupled with the conservation equations. Note that the current applications employ only pitch, heave, and roll motion, and the other three degrees of freedom are constrained.

For the translational motion, Newton's second law

$$m a_i = F_i \tag{10}$$

is solved in an absolute coordinate system, where F_i is an external force acting on the center of gravity, a_i is the acceleration and m is the mass of the rigid body. The external force is calculated by integrating the pressure, and viscous shear stresses over the rigid body's boundary

$$F_i = \int_A p\, dA + \int_A \mu \frac{\partial v_t}{\partial x_n}\, dA. \tag{11}$$

To obtain the translational velocity $\dot{r}_i$ and the position r_i of the rigid body's center of gravity, Eq. (10) is integrated over time.

To solve the rotational motion of the rigid body, the angular momentum equation is noted in local, body-fixed coordinates, leading to Euler's gyroscopic equations

$$M_1 = I_{11}\,\dot{\omega}_1 + \left(I_{33} - I_{22}\right)\omega_2\,\omega_3 \tag{12}$$

$$M_2 = I_{22}\,\dot{\omega}_2 + \left(I_{11} - I_{33}\right)\omega_3\,\omega_1 \tag{13}$$

$$M_3 = I_{33}\,\dot{\omega}_3 + \left(I_{22} - I_{11}\right)\omega_1\,\omega_2. \tag{14}$$

Here M_j are the moments acting from the fluid on the rigid body, obtained by integration over the rigid body's boundary, I_{ij} is the local inertia tensor which is constant, and ω_i is the local angular velocity and $\dot{\omega}_i$ is the local angular acceleration. A quaternion $\mathcal{P}_i$ including the four Euler parameters e_0, e_1, e_2 and e_3 is used to describe the rotational position, and a second quaternion $\dot{\mathcal{P}}_i$ is introduced to describe the rotational velocity. From Euler's gyroscopic Eqs. (12)–(14), the angular acceleration $\dot{\omega}_i$ is obtained and then integrated to the local angular velocity ω_i. The rotational velocity quaternion $\dot{\mathcal{P}}_i$ is then obtained by relation

$$\dot{\mathcal{P}}_i = \frac{1}{2} L_{ij}^T \omega_i, \tag{15}$$

where the matrix L_{ij} includes the Euler parameters

$$L_{ij} = \begin{bmatrix} -e_1 & e_0 & e_3 & -e_2 \\ -e_2 & -e_3 & e_0 & e_1 \\ -e_3 & e_2 & -e_1 & e_0 \end{bmatrix}. \tag{16}$$

Subsequently, $\dot{\mathcal{P}}_i$ is integrated into $\mathcal{P}_i$. More details on the implementation of the quaternion motion solver are described in Luo and Rung (2019, 2017), and a validation study of the six degrees of freedom solver is shown in Ulrich et al. (2013).

2.3. Wave generating boundary conditions

In the last 15 years, many successful proposals for the generation of complex far-field wave fields that can be embedded in Navier–Stokes simulations have been published, see for example Gentaz et al. (2004) or Jacobsen et al. (2012). The present approach follows a suggestion described in Wöckner et al. (2010). It is based on an implicit forcing of the discretized equations for the momentum (7) and (air) mixture fraction (1) in order to force frictionless representations of either linear (Airy) or nonlinear (Stokes) waves when approaching the far field. Moreover, different wave theories, e.g., JONSWAP Hasselmann et al. (1980), are available to generate complex wave fields from the superposition of individual wave components.

In the present work, the Airy theory is applied to generate exemplary linear, regular incident waves. They are derived from the deep water wave potential

$$\Phi = Re(-i\,c\,\hat{\xi} e^{(-kz)} e^{(\omega_w t - kx)}), \tag{17}$$

where c is the phase velocity of the wave, $\hat{\xi}$ denotes the wave amplitude, k represents the wave number and ω_w is the angular frequency of the wave. Here, t is the time, x denotes the direction of propagation of the wave, and z is the direction of wave elevation. The corresponding velocity components v_x and v_z are obtained by differentiating the wave potential w.r.t. x and z, respectively

$$v_x = \omega_w \hat{\xi} e^{(-kz)} \cos(\omega_w t - kx) \tag{18}$$

$$v_z = -\omega_w \hat{\xi} e^{(-kz)} \sin(\omega_w t - kx). \tag{19}$$

The air volume fraction follows from the free surface elevation ζ

$$\zeta(x,t) = \hat{\xi} \cos(\omega_w t - kx) \tag{20}$$

obtained by the dynamic and kinematic free surface conditions. The numerical implementation of the consistency of the viscous Navier–Stokes solution with the inviscid wave solution in the far field is described in Section 3.4.

3. Numerical method

The in-house solver FreSCo+, a joint development of Hamburg University of Technology (TUHH) and the Hamburgische Schiffbau Versuchsanstalt (HSVA), cf. Rung et al. (2009) is used as a framework to implement the monolithic granular cargo transport model.

In this section, the governing conservation equation system, the detailed discrete equations, the solution procedure and the treatment of the vessel motion, wave boundary conditions, and non-linear material property interpolation are discussed.

3.1. Solution procedure

A pressure-based FV formulation using a cell-centered, co-located variable arrangement on unstructured polyhedral grids, cf. for example, Ferziger and Perć (2008), is applied to discretize the governing equations for the mixture fractions (1), the momentum (7) and the displacement of the granular material (9). The segregated algorithm is completed by a SIMPLE-type pressure correction scheme, cf. Yakubov et al. (2015) and Völkner et al. (2017). For turbulent flows around a ship, the system is supplemented by two additional transport equations for the turbulent kinetic energy k and the specific energy dissipation ω together with wall-functions, to model the influence of turbulence (Wilcox, 2004).

The system of equations consists of the following equations for the conservation of momentum and mass

$$\begin{aligned} &\frac{d}{dt}\int_V (\rho v_i)dV + \oint_A \left(\rho\left(v_i - v_i^g\right)v_j\right)dA_j \\ &\quad = -\oint_A p dA_i + \int_V \rho g_i dV + \oint_A \mu\left(\frac{\partial\left(v_i - v_i^g\right)}{\partial x_j} + \frac{\partial\left(v_j - v_j^g\right)}{\partial x_i}\right)dA_j, \end{aligned} \tag{21}$$

$$\int_V \left(\frac{\partial\left(v_i - v_i^g\right)}{\partial x_i}\right)dV = 0, \tag{22}$$

as well as for the air and granular material mixture fraction

$$\frac{d}{dt}\int_V c_A\,dV + \oint_A \left(c_A\left(v_i - v_i^g\right)\right)dA_i = 0, \tag{23}$$

$$\frac{d}{dt}\int_V c_S\,dV + \oint_A \left(c_S\left(v_i - v_i^g\right)\right)dA_i = 0. \tag{24}$$

The arbitrary Eulerian Lagrangian (ALE) concept is applied, representing the convective fluxes using the mesh velocity v_i^g as further explained in Section 3.3. These equations are supplemented by the passive Eulerian transport equation for the displacement of the granular soil material

$$\frac{d}{dt}\int_V u_i\,dV + \oint_A c_S\left(v_j - v_j^g\right)u_i\,dA_j = \int_V \left(c_S\left(v_i - v_i^g\right)\right)dV. \tag{25}$$

After the integrals and derivatives have been approximated as described in Section 3.2, the procedure to solve the three-phase flow problem, including a granular phase, free surface waves, and a 6DoF rigid body motion, follows from Algorithm 1. The equations are solved in a segregated manner in a second outer iteration loop until a predefined residual threshold is obtained within each time step.

3.2. Numerical approximation

Temporal derivatives are either approximated by a first-order accurate implicit method (verification and validation cases) or a second-order accurate implicit three time-level scheme (application case). Spatial integrals are approximated by a second-order accurate mid-point rule. Diffusive fluxes are approximated using a central differencing scheme (CDS). The approximation of convective fluxes utilizes a flux blending scheme, where 70 % of the contributions originate from the

Algorithm 1 Incompressible three-phase flow including granular phase coupled with rigid-body motion and waves.

Initialize v_i^0, p^0, c_A^0, c_S^0, u_i^0, ρ^0, μ^0, a_i^0, $\dot{r}_i^0$, r_i^0, $\dot{\omega}_i^0$, ω_i^0
$n = 0$
$m = 0$
while $n \leq$ max. number time steps **do** ▷ n denotes the current time step
  $n = n + 1$
  while residual < residualThreshold **do** ▷ m denotes the number of outer iterations
    $m = m + 1$
    update properties ▷ Eqs. (4), (3)
    calculate fluid forces and moments on rigid body ▷ Eq. (11)
    solve equations of motion
    ▷ Eqs. (10), (12), (13), and (14)
    move grid
    solve momentum equations ▷ Eqs. (21), (37)
    solve first stage of pressure correction equation ▷ cf. Düsterhöft-Wriggers et al. (2024)
    correct pressures, fluxes and velocities ▷ cf. Düsterhöft-Wriggers et al. (2024)
    solve second stage of pressure correction equation ▷ cf. Düsterhöft-Wriggers et al. (2024)
    correct pressures ▷ cf. Düsterhöft-Wriggers et al. (2024)
    solve air mixture fraction equation ▷ Eqs. (23), (37)
    solve soil mixture fraction equation ▷ Eq. (24)
    solve displacement equations ▷ Eq. (25)
  end while
  v_i^n, p^n, c_A^n, c_S^n, u_i^n, ρ^n, μ^n, a_i^n, $\dot{r}_i^n$, r_i^n, $\dot{\omega}_i^n$, ω_i^n
$\rightarrow$ v_i^{n-1}, p^{n-1}, c_A^{n-1}, c_S^{n-1}, u_i^{n-1}, ρ^{n-1}, μ^{n-1}, a_i^{n-1}, $\dot{r}_i^{n-1}$, r_i^{n-1}, $\dot{\omega}_i^{n-1}$, ω_i^{n-1}
end while
update properties ▷ Eqs. (4), (3)
return v_i^n, p^n, c_A^n, c_S^n, u_i^n, ρ^n, μ^n, a_i^n, $\dot{r}_i^n$, r_i^n, $\dot{\omega}_i^n$, ω_i^n ▷ defined at output time steps

second-order accurate CDS and 30 % from the first-order upwind scheme (UDS). Except for this, the approximation of the convective flux in the mixture fraction equations follows the Quadratic Upstream Interpolation for Convective Kinematics (QUICK) scheme, initially introduced by Leonard (1979).

The applied finite volume (FV) method discretizes the equations, which are formulated in integral form, by dividing the computational domain into finite control volumes of size ΔV_P. The center of each control volume is denoted as $_P$, while the values at the faces are indicated as $_f$; these are necessary for discretizing the surface integrals. In the following sections, A represents the face area, and A_i is the outward-pointing face vector. The scalar distance between the cell center and the adjacent neighboring centers is labeled as d, with its corresponding vector denoted as d_i. A time step size of Δt is utilized, and g_i refers to the acceleration due to gravity acting on the system.

3.2.1. Momentum equations

The discrete form of the momentum equations get

$$\begin{aligned} v_{i,P}^{n,m} \underbrace{\left[\Delta V_P \frac{\rho_P}{\Delta t} + \sum_{f(\Delta V_P)} A_{NB}^{v_i}\right]}_{A_P^{v_i}} \\ - \sum_{f(\Delta V_P)} \underbrace{\left[\left(\max\left[-\dot{m}^{n,m-1}, 0\right]\right)_f + \left(\frac{\mu A}{d}\right)_f\right]}_{A_{NB}^{v_i}} v_{i,NB}^{n,m} \\ = - \sum_{f(\Delta V_P)} \left(p_f^{n,m-1} A_i\right) + \rho_P \Delta V_P \left(g_i + \frac{v_i^{n-1}}{\Delta t}\right)_P + S_{v_i}, \end{aligned} \tag{26}$$

when using a mid-point integration rule together with the first-order implicit time discretization and an implicit upwind-difference scheme for the convective flux. Here $\dot{m}_f = (\rho(v_i - v_i^g)A_i)_f$ refers to the mass flux and S_{v_i} to a term including deferred-corrections.

3.2.2. Pressure correction equations

The SIMPLE-type pressure correction scheme derivation is based on the continuity and linearized momentum equations. Here, p' denotes the pressure correction, and the pressure correction equation

$$\sum_{f(\Delta V_P)} \left(v_{f,i}^m - v_{f,i}^{g,m}\right) A_{f,i} - \sum_{f(\Delta V_P)} \left(\frac{A_i d_i}{A_P^{v_i}}\right)_f \left(\frac{\partial p'}{\partial x_i}\right)_f A_f = 0, \tag{27}$$

is solved in two stages. In the first stage, the partial derivative of the pressure is discretized as

$$\left(\frac{\partial p'}{\partial x_i}\right)_f = \left(\frac{p'_{NB} - p'_P}{d}\right) \tag{28}$$

leading to

$$\sum_{\Delta V_P} \left[\underbrace{\left(\frac{A_i d_i}{A_P^{v_i} d}\right)_f}_{A_P^{p'}} p'_P + \sum_{NB} \underbrace{-\left(\frac{A_i d_i}{A_P^{v_i} d}\right)_f}_{A_{NB}^{p'}} p'_{NB} = -\dot{v}_{\Delta V_P}^m\right]. \tag{29}$$

The pressure p^{m-1} is updated to p^m with the obtained pressure correction p' ($p^m = p^{m-1} + p'$) afterwards. The velocity and fluxes are corrected via

$$v_{i,P}^{m*} = v_{i,P}^m + \left(-\frac{\Delta V_P}{A_P^{v_{i,P}}}\right)\left(\frac{\partial p'}{\partial x_i}\right)_P \tag{30}$$

and

$$\dot{v}_f^{m*} = \dot{v}_f^m + A_{NB}^{p'}\left(p'_{NB} - p'_P\right) \tag{31}$$

respectively. For the collocated variable arrangement, the Rhie and Chow (1983) interpolation of the fluxes is used to avoid pressure oscillations.

In the second stage of the pressure correction algorithm, non-orthogonal terms are included in the pressure's partial derivative

$$\left(\frac{\partial p'}{\partial x_i}\right)_f = \left(\frac{p'_{NB} - p'_P}{d}\right) + \left(\frac{\partial p'}{\partial x_i}\left(\frac{A_i}{A} - \frac{d_i}{d}\right)\right)_f. \tag{32}$$

After solving the second system of equations for the pressure correction, the pressure, fluxes, and velocities are updated again.

3.2.3. Mixture fraction equations

Employing a first-order implicit time integration scheme alongside an implicit upwind difference scheme to approximate the convective term in the mixture fraction equations, the discrete forms of the soil and air mixture fraction equation are given by

$$\underbrace{c_{S,P}^{n,m}\left[\frac{\Delta V_P}{\Delta t}+\sum_{f(\Delta V_P)}A_{NB}^{c_S}\right]}_{A_P^{c_S}}-\sum_{f(\Delta V_P)}\underbrace{\left(\max\left[-(\dot{m}/\rho),0\right]\right)_f}_{A_{NB}^{c_S}}c_{S,NB}^{n,m} = \frac{\Delta V_P}{\Delta t}c_{S,P}^{n-1}+S_{c_S}, \tag{33}$$

$$\underbrace{c_{A,P}^{n,m}\left[\frac{\Delta V_P}{\Delta t}+\sum_{f(\Delta V_P)}A_{NB}^{c_A}\right]}_{A_P^{c_A}}-\sum_{f(\Delta V_P)}\underbrace{\left(\max\left[-(\dot{m}/\rho),0\right]\right)_f}_{A_{NB}^{c_A}}c_{A,NB}^{n,m} = \frac{\Delta V_P}{\Delta t}c_{A,P}^{n-1}+S_{c_A}. \tag{34}$$

The term S_c includes the deferred correction terms for the compressive approximation, allowing us to calculate the mass flux $\dot{m}$ from the corrected flux $\dot{v}^{m*}$.

3.2.4. Displacement equation

For a first-order implicit time integration scheme and an implicit upwind-difference scheme for the convective term, the discrete form of the Eulerian displacement equation gets

$$\underbrace{u_{i,P}^{n,m}\left[\frac{\Delta V_P}{\Delta t}+\sum_{f(\Delta V_P)}A_{NB}^{u}\right]}_{A_P^{u}}-\sum_{f(\Delta V_P)}\underbrace{\left(\max\left[-\dot{v}^{S,n,m-1},0\right]\right)_f}_{A_{NB}^{u}}u_{i,NB}^{n,m} = \frac{\Delta V_P}{\Delta t}u_{i,P}^{n-1}+c_{S,P}v_{i,P}^{n,m-1}\Delta V_P+S_u. \tag{35}$$

Here, $\dot{v}_f^S=(c(v_i-v_i^g)A_i)_f$ represents the flux, and S_u includes explicit terms that arise from various deferred correction contributions, such as higher-order convection, non-orthogonality, and interpolation corrections.

3.3. Vessel motion

Using a 6DoF rigid-body motion solver, several options are conceivable to implement the mesh motion associated with the motion of the hull. Next to overset grids as described in Völkner et al. (2017), deformed meshes as in Manzke (2019), or rigid mesh motions can be employed. The present study opts for the rigid mesh motion. To this end, the mesh moves with velocity v_i^g, which follows from the translational and angular velocity of the rigid vessel, and the governing equations for a property $\phi=v_i,u_i,c_S,c_A,k,\omega,1,\ldots$ follow the arbitrary Eulerian Lagrangian (ALE) concept, i.e. the convective fluxes are formulated using the relative velocity, i.e., $\partial(\phi(v_j-v_j^g))/\partial x_j$ in Section 2.1.2.

3.4. Wave boundary conditions

As described in Wöckner et al. (2010), the implementation of the boundary conditions is carried out in an implicit manner within the algebraic equation system that follows from the finite volume discretization. Thereby, the algebraic equation system of the variables directly linked to the sea state in the far field is manipulated, i.e. the equations for the velocities and the mixing fraction of the water or air phase. Using a generic algebraic equation to determine the variables $\Theta=u,v,w,c_A$ or c_W

$$A_P^{\Theta}\,\Theta_P+\sum_{NB}A_{NB}^{\Theta}\,\Theta_{NB}=S_P^{\Theta}, \tag{36}$$

where the subscripts A_P, A_{NB} represent the main diagonal of the coefficient matrix $\mathbf{A}$ and the corresponding off-diagonal entries and S_P^{Θ} denotes the right-hand side of the equation for the CV centered around P. The manipulation aims to drive the far-field solution Θ_P towards an inviscid wave field Θ_P^*, cf. Section 2.3, and is carried out as follows:

$$\left[1+\beta_w\,\alpha_w(x_w)\right]\,A_P^{\Theta}\,\Theta_P+\sum_{NB}A_{NB}^{\Theta}\,\Theta_{NB}=S_P^{\Theta}+\left[A_P^{\Theta}\,\beta_w\,\alpha_w(x_w)\,\Theta_P^*\right]. \tag{37}$$

The factor β_w is a constant of order 10^{-3} and the function α_w depends on the distance Δ to the nearest far-field point, e.g.,

$$\alpha_w=\left(1-\frac{\Delta}{d}\right)^3, \tag{38}$$

where d is the width of the transition zone, cf. Fig. 2.

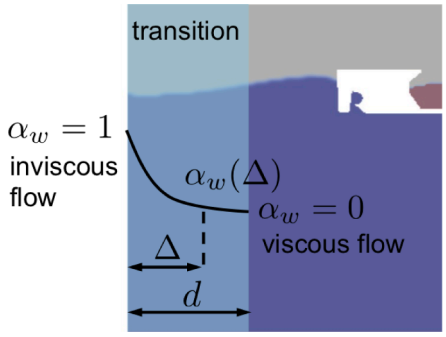

Fig. 2. Illustration of the far-field wave boundary condition.

3.5. Non-linear interpolation of material properties

The applied non-linear interpolation for the material properties of density and viscosity uses an arctan function. In this context, γ symbolizes a general property, while superscripts ^{A} and ^{S} refer to the air/water and soil phases, respectively. The constant N allows for control over the sharpening of the interpolation. The interpolation function is expressed as follows

$$\begin{aligned}\gamma=\gamma^A&+\left(\frac{\arctan\left(N\left(c_S-0.5\right)\right)}{\pi}+0.5\right)\left(\gamma^S-\gamma^A\right)\\&-\left(1-c_S\right)\epsilon_0\left(\gamma^S-\gamma^A\right)+c_S\,\epsilon_1\left(\gamma^S-\gamma^A\right)\\&-\left(1-c_S\right)\delta_0\left(\gamma^S-\gamma^A\right)\end{aligned} \tag{39}$$

with

$$\epsilon_0=\frac{\arctan\left(-0.5N\right)}{\pi}+0.5, \tag{40}$$

$$\epsilon_1=0.5-\frac{\arctan\left(0.5N\right)}{\pi}, \tag{41}$$

as well as

$$\delta_0=\left(\frac{\arctan\left(-0.5\;N\right)}{\pi}+0.5\right)-\epsilon_0. \tag{42}$$

4. Validation and verification studies

Prior to a complex 3D ship application, two components of the model are validated and verified. Two-phase flow validations for the same FV framework can be found in Manzke (2019), Kühl et al. (2021) and Düsterhöft-Wriggers et al. (2022). Moreover, the rigid body motion solver and the wave-generating boundary conditions are validated in Luo and Rung (2019) and Luo and Rung (2017), respectively. However, since the presented three-phase flow model has not yet been validated, this is done here using a case that complements the validations outlined in Düsterhöft-Wriggers et al. (2024), which is of significance for the complete 3D problem of granular cargo transport. In addition, the efficiency of the non-linear interpolation of material properties for a granular material model within a FV framework is demonstrated using another 2D case that observes the collapse of a granular column.

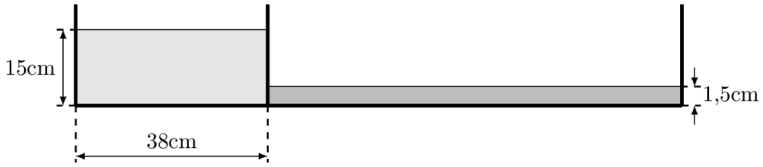

Fig. 3. Initial geometry of three-phase dam break experiments by Jánosi et al. (2004).

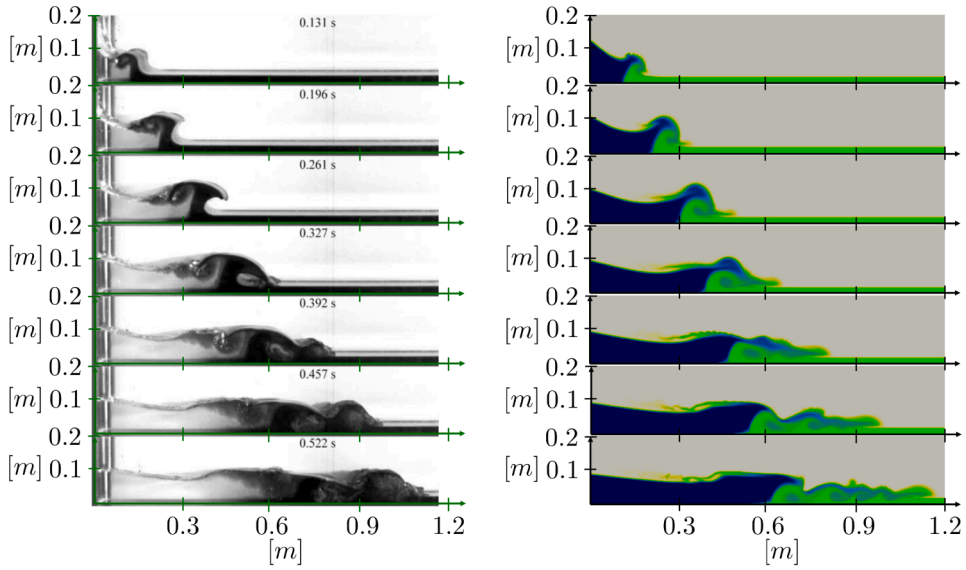

Fig. 4. Snap shots of experimental results from Jánosi et al. (2004) and numerical results from the present three-phase Volume of Fluid method.

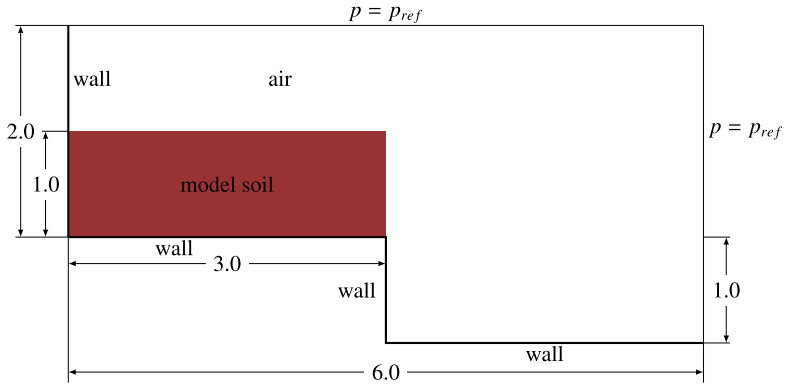

Fig. 5. Initial set up of 2D soil dam breaking down a step test case by Larese (2012) with measurements given in meters.

4.1. Three-phase flow

To validate the three-phase flow model, a dam break experiment by Jánosi et al. (2004), where a higher column of clear water breaks into a layer of colored water, is used as a reference. Besides the clear and colored water, air is considered the third phase in the present model. The dimensions of the initial state, in which the clear water is separated from the colored water by a floodgate, of the experiment are displayed in Fig. 3. The rectangular computational domain is chosen to have a height of $h = 0.2$ m and a width of 1.2 m with a cell size of $\Delta x_1 = \Delta x_2 = h/100$. At the beginning of the experiment, the floodgate is pulled up, and a time step of 10^{-3} s is used for the simulations. The results obtained from the present method are visually compared with the experimental data in Fig. 4. In this figure, grey denotes air, green represents the colored water, and blue signifies the clear water.

The numerical results demonstrate high concordance with the experimental data regarding the front position across all time steps. However, a notable divergence in breaking behavior is observed at $t = 0.131$ s, attributable to the floodgate opening mechanism in the experimental setup, which is not replicated in the numerical simulations. The velocity profile within the dam exhibits discrepancies when comparing the floodgate opening scenario to the free-breaking dam simulation. Specifically, the numerical results indicate a higher rightward velocity at the dam's apex than the experimental observations. Consequently, a greater proportion of clear water is discernible at the dam's crest in the numerical results, a phenomenon that persists throughout subsequent time steps.

The three-phase VoF method yields a less pronounced representation of the breaking water-free surface morphology at $t = 0.196$ s and $t = 0.261$ s relative to the experimental findings.

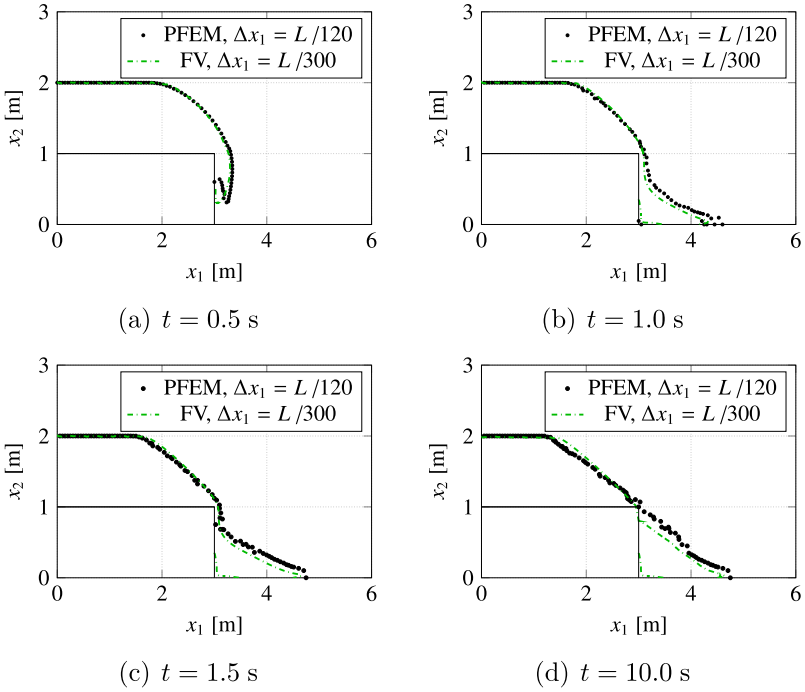

Fig. 6. Comparison of the temporal soil-surface evolution predicted by the present FV approach with linear interpolation of the material properties and the PFEM approach of Larese (2012) for the collapse of a 2D soil dam over a backward-facing step.

4.2. Granular material

The second verification case refers to the collapse of a soil dam for various angles of repose. Results of the present approach are compared against results obtained from a particle Finite Element Method (PFEM) following the methodology introduced by Larese (2012). The configuration consists of a soil dam with dimensions of 3 m width and 1 m height, positioned on a step with a width of 3 m. The dam is released at $t = 0.0$ s, initiating the observation period. Fig. 5 illustrates the initial geometry and boundary conditions of the experiment, where the total length L of the computational domain is 6.0 m.

Following Larese (2012), artificial material properties are used, i.e. a soil density of $\rho^S = 1000\,\mathrm{kg/m^3}$, a minimum soil viscosity of $\mu^S_{\min} = 10^{-6}$ Pa s, an angle of repose of $\phi = 30°$ and a reference pressure of $p_{ref} = 0.0$ Pa. Furthermore, for better comparability, the yield criterion does not follow from the numerator $3\alpha_\phi p + k_c$ in (4), but employs the yield function Φ used in Larese (2012)

$$\Phi = \sqrt{J_2} - p\,tan\,\phi - C, \tag{43}$$

which involves the second invariant of the deviatoric stress J_2. Therefore, the main difference between the applied granular models lies in their discretization methods and the consideration of single-phase (Larese, 2012) versus two-phase (present study) problems.

Figs. 6 and 7 compare the results obtained from the present FV method with the results obtained from the PFEM approach reported by Larese (2012), where the present approach employs the non-linear interpolation of density and viscosity given in Section 2.1.1. To demonstrate the effectiveness of nonlinear interpolation of material properties, the results of the present FV method are compared against the results obtained from the PFEM approach with two different mesh resolutions. In Fig. 6, the present FV method using linear material interpolation and a cartesian grid featuring $\Delta x_1 = \Delta x_2 = L/300$ displays a reasonable agreement of the temporal soil-surface evolution with the PFEM approach on a coarser triangular grid with edge length $\Delta x_1 = L/120$. Using the non-linear interpolation function (39), however, improves the results and yields to a better matching soil-surface evolution when compared to an even finer triangular grid with edge length $\Delta x_1 = L/600$ for the PFEM approach, cf. Fig. 7. The PFEM reference results on the fine grid with $\Delta x_1 = L/600$ were obtained by a mesh convergence study and present the best representation of the physical problem. Also, mesh convergence studies were undertaken for the displayed FV results, leading to the applied grid sizes for the linear and non-linear interpolated material properties.

Besides demonstrating the benefits of the non-linear material property interpolation, the key observations are that the granular model discretized with the current approach exhibits more adhesion to the wall during the flow process. Despite the different wall adhesion, both methods show excellent agreement in their overall results.

5. 3D bulk carrier in waves loaded with granular material

The sinking of the "Jian Fu Star" occurred on 27th October after 21 hours of high Northerly winds between 5 and 8 Beaufort. The vessel had a length over all of $LoA = 189.9$ m, a width of $B = 31.2$ m, a summer draught of 11.43 m and metacentric height of $GM = 5.0$ m. At the time of the accident, the vessel transported Indonesian nickel ore in all five of its cargo holds. As described by the survivors (Investigation Department, 2011), the ship's roll motion was initially moderate, but it was pitching heavily and green water entered the forward deck. To avoid engine surcharge, the speed of the vessel was reduced to 4.5 kn, after which it suddenly began to list about 5° to port. As a countermeasure, pumping of ballast water was started. However, the measure did not have the desired effect, and the vessel began to list even more, up to 10°. The vessel then rolled around this list angle, took on high seas on board and sank 20 min after the first list had occurred. Twelve sailors were rescued and thirteen sailors were lost.

A generic bulk carrier hull geometry was selected to perform the numerical studies and scaled to meet the main dimensions of the "Jian Fu Star", resulting in a draft of $D = 11.8$ m, a freeboard of $F = 6.7$ m and a length between perpendiculars of $L_{PP} = 183.0$ m. Cargo holds with the dimensions given in Figs. A.19, A.20, and A.21 were added to the hull geometry, corresponding to the arrangement of the cargo compartments of the "Jian Fu Star" as given in Fig. A.18. Unlike in reality, the cargo holds were not closed with lids but connected to the air, creating a contiguous

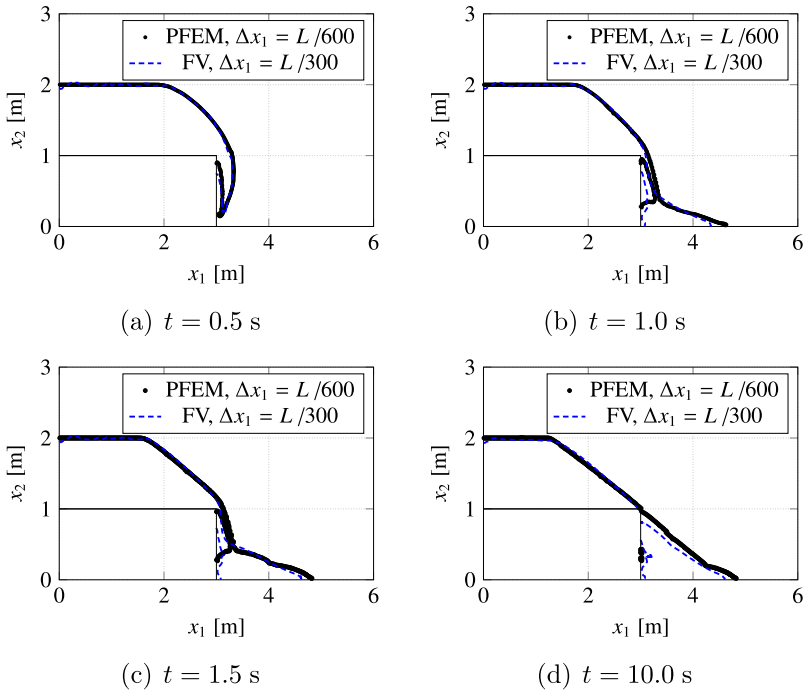

Fig. 7. Comparison of the temporal soil-surface evolution predicted by the present FV approach with non-linear interpolation ($N = 25$) and the PFEM approach of Larese (2012) for the collapse of a 2D soil dam over a backward-facing step.

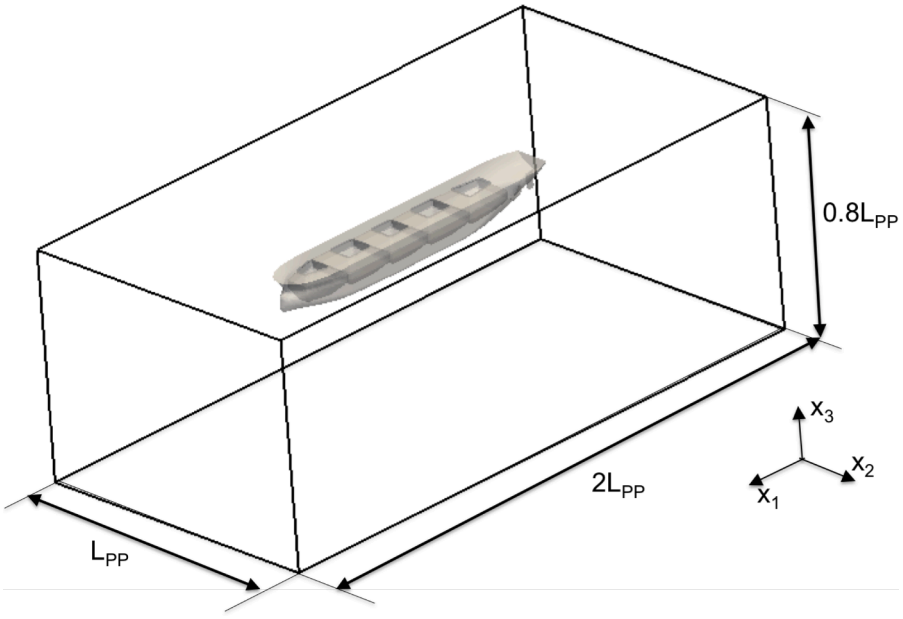

Fig. 8. Computational domain and bulk carrier geometry utilized for the 3D cargo-loaded vessel in seaway simulation.

domain to solve the conservation equations. To reconstruct the loading conditions, the soil fraction was initialized according to the stowage plan outlined in the accident investigation report of the "Panama Maritime Authority" (Investigation Department, 2011), cf. Fig. A.18. The investigated geometry and the dimensions of the computational domain in relation to the length between perpendiculars are displayed in Fig. 8. Details of the initial position of the three-phase continuum consisting of air, water and granular phases, are given in Fig. 9.

As given in the incident report (Investigation Department, 2011), the moisture content MC was certified to be 34.45 %, and the measured particle size did not exceed 200 mm. Since no further test on the material's properties was repeated directly before the "Jian Fu Star" 's departure, the incident report (Investigation Department, 2011) concludes that a higher MC during carriage cannot be excluded. In the present simulation, the cargo properties were selected to match Indonesian nickel ore with a MC of 29 % to use a conservative estimate of the material properties. The employed properties were extracted from the table of the material properties of the "Guidelines for Safe Carriage of Nickel Ore" published by the Class NK Japan classification society (ClassNK, 2012). Accordingly, the angle of repose ϕ is set at 4°, the cohesion C is set as 7900 Pa and the cargo density is set to the wet density of 1700 kg/m^3. The cargo behavior follows the rigid-perfectly plastic

(a) Longitudinal section through bulk carrier (b) Cross-section through bulk carrier

Fig. 9. 3D cargo vessel in waves: Initialization of granular cargo (red), water (blue), and air phases (light grey) displayed in two different cutting planes of the computational domain.

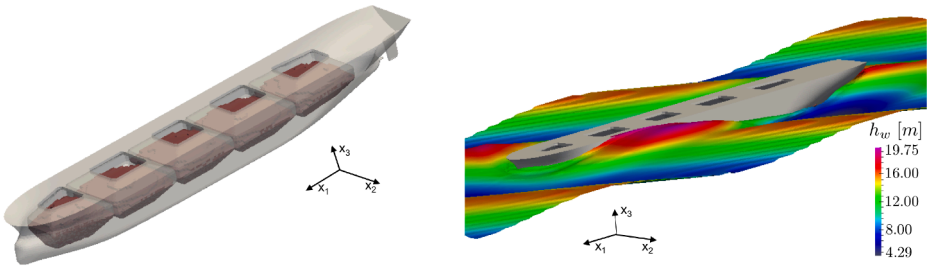

(a) Bulk carrier geometry with initialized cargo (b) Free surface height h_w

Fig. 10. 3D cargo vessel in waves: Loaded bulk carrier geometry and wave conditions at an early time step. The free surface height h_w of the water phase refers to the origin of the coordinate system positioned at the bottom of the vessel hull.

Table 2
Data of empty bulk carrier model "Jian Fu Star" in incident study.

m (mass)	13634.643 t
CoG (center of gravity)	(92.875|0.0|8.497) m
I_{11} (moment of inertia)	3.3548749750×10^9 kg m^2
I_{22} (moment of inertia)	$4.0278141357 \times 10^{10}$ kg m^2
I_{33} (moment of inertia)	$4.5380647175 \times 10^{10}$ kg m^2
$I_{23} = I_{32}$ (moment of inertia)	$-4.3608019573 \times 10^7$ kg m^2

approach with the Drucker-Prager yield criterion given in Section 2.1.2. The density of air and seawater are set to $\rho^A = 1.185\,\text{kg/m}^3$ and $\rho^W = 1025\,\text{kg/m}^3$ and the employed viscosities read $\mu^A = 1.831 \times 10^{-5}$ Pa s and $\mu^W = 1.132 \times 10^{-3}$ Pa s for the air and the water phase, respectively. The non-linear interpolation of the granular phase with the other phases is applied with a constant of $N = 5$.

A three-degree-of-freedom (3DoF) rigid body motion of the vessel is assumed, where the vessel can heave, pitch, and roll. The ship properties used to control rigid body motion include the position of the center of gravity, the mass, and the moments of inertia of the bulk carrier. In this study, the simulated vessel refers to an empty hull, and the cargo is realized by a continuum whose mass acts on the ship as a pressure force. Therefore, the data for the empty bulk carrier, cf. Table 2, is derived by subtracting the properties of the cargo from the fully loaded bulk carriers' properties obtained from hydrostatic formulas, the vessel data given by the incident report, and the generic hull model. As displayed in Fig. 9, the mean level of the free surface is initialized at the height of 11.8 m, in line with the departure draft D. Estimated from the weather conditions reported in the accident report, an Airy wave with a height of 8 m and length of $0.57L_{PP}$ was used as a far-field wave boundary condition, cf. Section 2.1.2. Since the vessel was sailing to the north-east and the wind direction is reported as northerly, the waves are assumed to hit the bulk carrier diagonally from the front with an angle of 48° towards the vessel's longitudinal axis. Fig. 10 depicts an early simulation time of the vessel in waves.

The study employed an unstructured hexahedral mesh with 9.07 Mio cells used, featuring in an averaged edge size of $\Delta x_1 \approx L_{PP}/184$. The mesh is evenly distributed due to the expected large rotations of the vessel, where the entire mesh is moved due to rigid body motions. An implicit Crank–Nicholson time discretization is applied to all equations with a time step of 10^{-4} s. To counteract the numerical diffusion induced by the coarse mesh resolution, a non-linear interpolation method described in Düsterhöft-Wriggers et al. (2024) is applied to sharpen the material properties at the soil-air interface.

Turbulence is modeled using a $k-\omega$ eddy-viscosity model in combination with wall functions. The horizontal and lateral boundaries are assigned to the far-field conditions described in Section 2.3. The bottom-plane horizontal boundary is assigned to Dirichlet conditions for the velocity and the top plane follows from a fixed ambient pressure boundary condition. Based on the incident report, a vessel speed of 4.5 kn is assumed, resulting in a Froude number of $Fn = 0.055$ and a Reynolds number of $Re = 3.8 \times 10^8$.

The hydrodynamic response of a cargo-loaded vessel subjected to wave-induced motions was computationally simulated for 40 s. The simulation required approximately 2×10^5 CPUh on an HPC-system.

5.1. Results of 3D feasibility study with rigid perfectly-plastic cargo

In Fig. 11, the viscosity of the cargo calculated using the Drucker-Prager yield criterion is visualized for regions where the soil mixture fraction is between 0.95 and 1.0. At time $t = 3.0$ s, the cargo loading configuration results in circular patterns of lower viscosity, indicative of the cargo's propensity to spread and flatten at the beginning of the simulation. As the simulation progresses to $t = 18.5$ s, the cargo has already experienced a significant flattening of the hill-shaped initial state. At the same time, the vessel's pitch motion induces high accelerations in hold one, and the viscosity exhibits a longitudinal gradient, with the lowest values observed in the forward hold progressively increasing towards the aft. This general trend persists in subsequent time steps. At

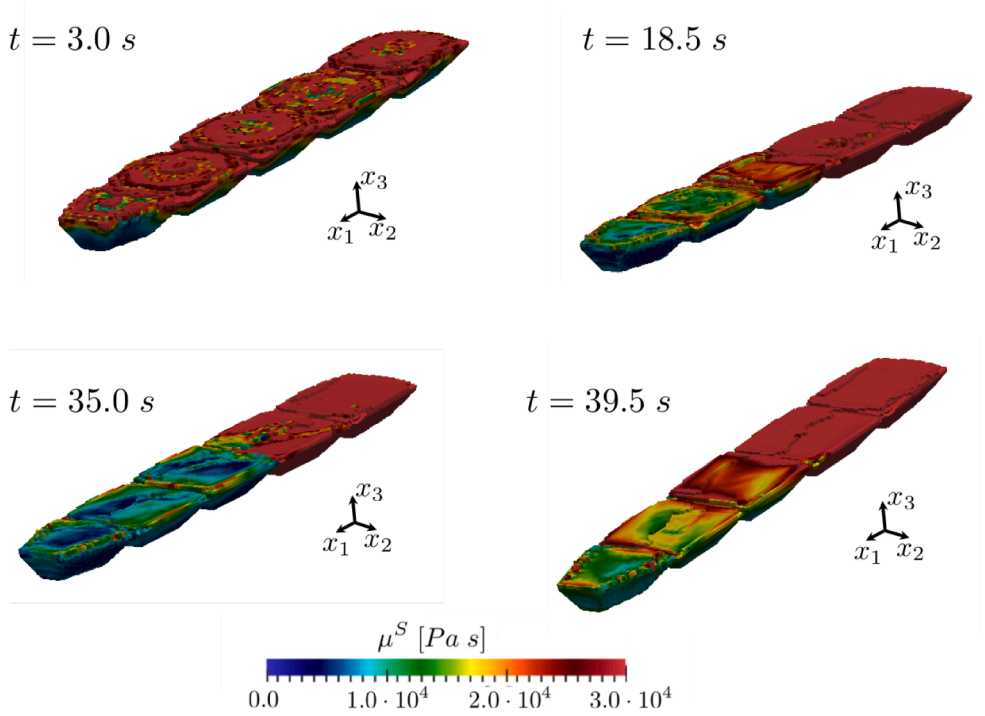

Fig. 11. Snap shots of the nickel ore cargo-phase viscosity using the rigid perfectly-plastic cargo model extracted at four times during voyage in waves.

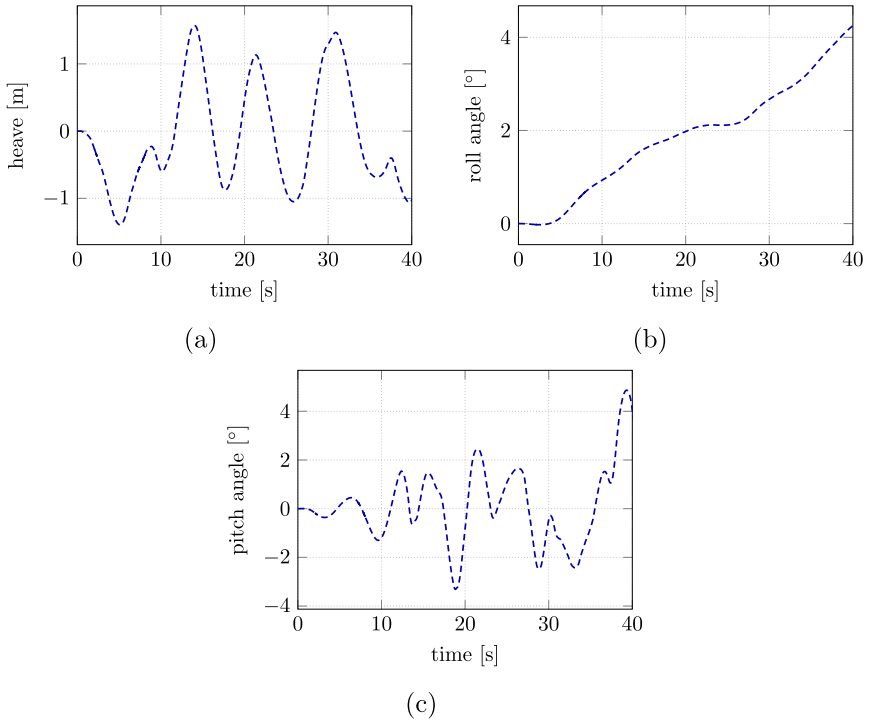

Fig. 12. Time evolution of the nickel ore loaded vessel's heave, roll and pitch motion during the voyage in waves, using the rigid perfectly-plastic cargo model.

the time $t = 35.0$ s, a cargo sliding plane can be observed in hold four, and generally, a cargo shift can be observed at the top of the cargo piles. This shift stays prominent until time $t = 39.5$ s, where a slight shift to the front of the vessel can also be detected. The spatial and temporal variations in viscosity can be attributed to several factors, i.e., the initial cargo distribution, gravitational effects, the vessel's motion as well as the interaction between the cargo and the hold structures.

The 3DoF motions exhibited by the vessel during the simulation are illustrated in Fig. 12. The heave fluctuates around zero, cf. Fig. 12(a), where the pitch, cf. Fig. 12(c), and roll angle, cf. Fig. 12(b), behave less periodically. The pitch angle peaks at 39.3 s where the vessel's bow is shortly before diving below the free surface. It is assumed that the vessel would sink over the bow for a longer simulation. The rolling motion constantly increases during the simulation. This is thought to be attributed to the cargo shift occurring just at the beginning of the simulation when the cargo heaps flatten. A shift of the cargo can be observed already before $t = 15.5$ s as indicated in Fig. 15, which leads to vessel instability. Two of the snapshots presented in Fig. 11 were selected to depict the vessel's orientation at the extreme values of its pitch angle oscillations ($t = 18.5$ s and $t = 35.0$ s). The observed progressive rolling motion

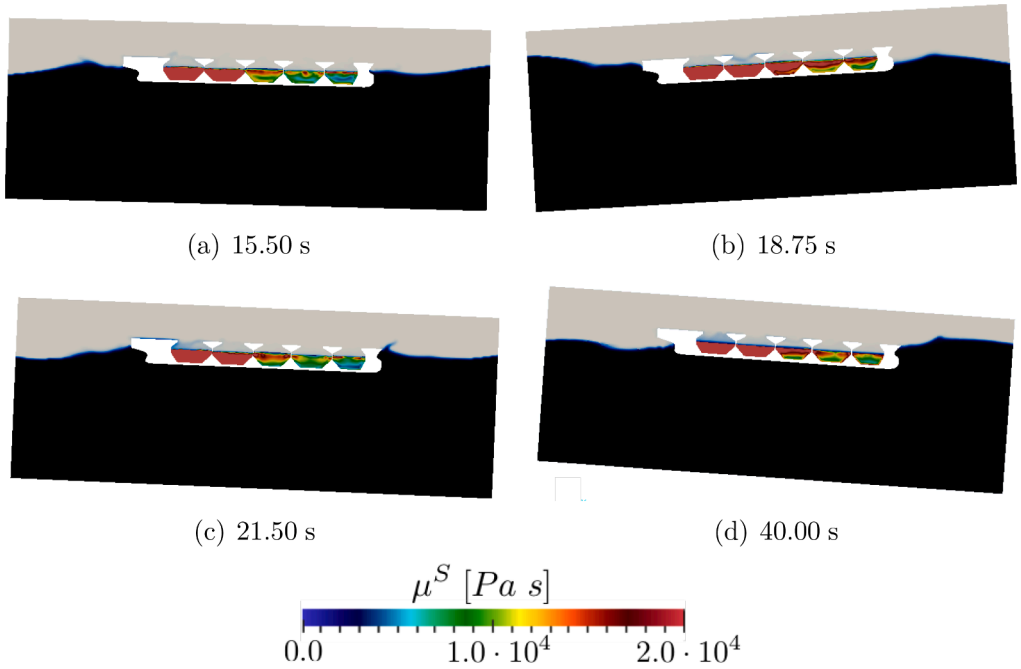

Fig. 13. Snap shots of the nickel ore cargo-phase viscosity extracted in an $x_1 - x_3$ cutting plane at $x_2 = 0$ m at four times during the voyage in waves. Black regions denote the water phase, while the grey regions indicate the air phase. Mind that the domain dynamically rotates according to the vessel's rigid body motion.

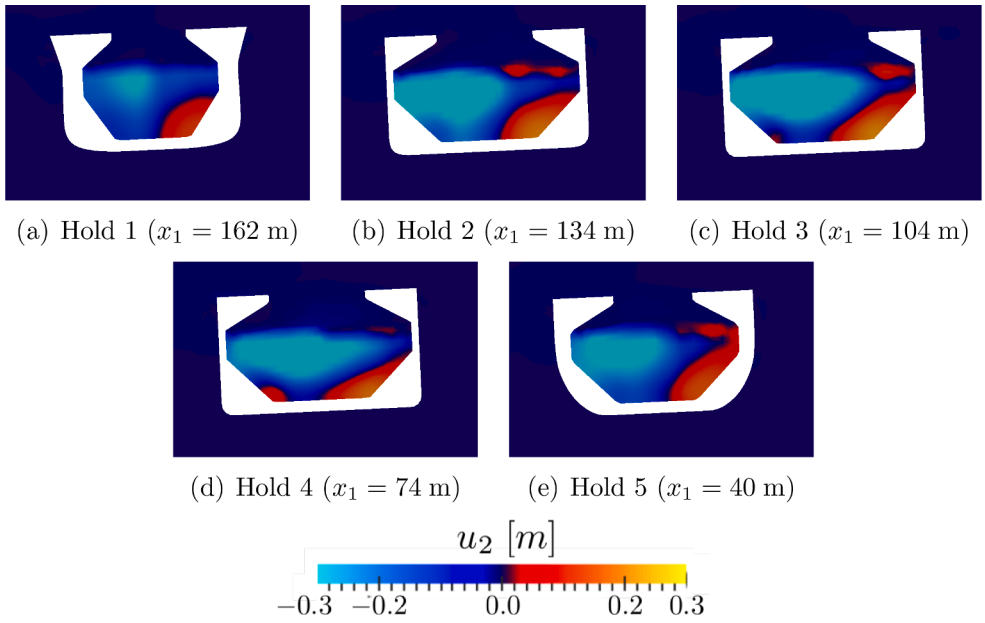

Fig. 14. Cargo displacement in the ship's lateral x_2-direction displayed for the central cross section of all five holds of the nickle ore loaded vessel in seaways at time $t = 30.0$ s.

of the vessel suggests a high probability of cargo shifting, potentially leading to capsizing. Upon closer inspection of the topmost cells shown in Fig. 11, a subtle but noticeable cargo shift towards the starboard side becomes visible, starting at about 15.5 s.

The temporal evolution of the viscosity distribution within the cargo holds in a cutting plane defined by $x_2 = 0$ m is illustrated in Fig. 13. For the last three time instants $t = 18.75$ s, $t = 21.5$ s, and $t = 40.0$ s, it is evident that the ship is taking on water, as can also be observed in Fig. 17. This observation aligns with the incident report of the "Jian Fu Star", although it should be noted that, in reality, the holds were equipped with lids that did prevent water from sloshing into the holds. Due to the immiscible formulation of the cargo model, this water ingress does not affect the cargo properties. Nevertheless, a free surface inside the cargo holds can be observed at time $t = 40.0$ s, that admittedly affects the vessel stability. However, in any case a larger influence of the displacement of the highly dense granular material on the stability is observed. Fig. 13 also reveals that the cargo exhibits softer behavior in the forward holds. This phenomenon is particularly pronounced when the vessel is pitching downward, as exemplified by the pitch angle maxima at $t = 21.5$ s, where the viscosity reaches its minimum at the bottom of hold one.

Lee's study (Lee, 2017) on the vessel "Alam Manis", which traversed a typhoon, provides a detailed account of cargo consistency in each hold. The findings of that study corroborate the results of the present

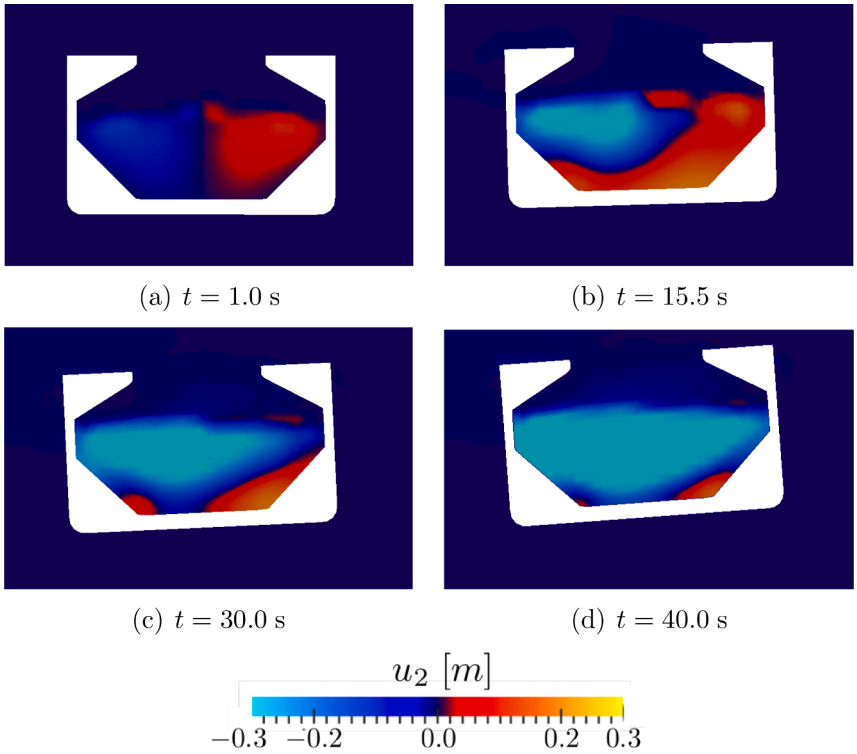

Fig. 15. Cargo displacement in the ship's lateral x_2-direction displayed for the central cross section of hold 4 of the nickle ore loaded vessel in seaways during four time steps.

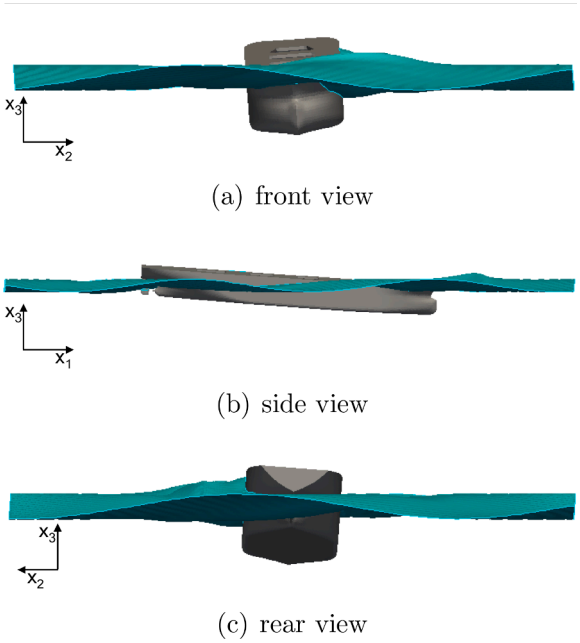

Fig. 16. Snap shots of the bulk carrier at time $t = 40.0$ s from the front, side and rear view.

feasibility study. Specifically, the highest accelerations were observed to act on the cargo in the forward holds, with the most significant cargo shifts occurring in hold one. Lee (2017) reported a gradual decrease in cargo shift angle from the forward to the aft holds. Furthermore, the IMO "Technical Working Group" (Iron Ore Technical Working Group, 2013) confirms that the highest accelerations during bulk carrier voyages were recorded in the forward hold, which is consistent with the results presented in this study.

In Fig. 14, the lateral component of the Eulerian cargo displacement is visualized in the central cross section of each hold at time $t = 30.0$ s. The most substantial displacement is manifested in holds two and three, specifically in the central regions of these cargo compartments. This can be attributed to the geometric constraints imposed by the hold structures and the reduced viscosity in the central areas of the holds, as evidenced in Figs. 11 and 13. To elucidate the impact of the vessel's successive rolling motion on the cargo, Fig. 15 presents the lateral component of the Eulerian cargo displacement at four distinct times extracted in a central cross section of the fourth hold. At $t = 15.5$ s, $t = 30.0$ s and $t = 40.0$ s, a notable shift towards starboard (indicated by negative displacement) is observed. Over time, the corresponding zero line of displacement migrates increasingly towards the vessel's port side, i.e. the right side in Fig. 15.

The final position of the bulk carrier in the simulation is depicted in Fig. 16 for three different views, i.e., front, rear, and side view. The severe pitch of the vessel, which could induce sinking over the nose, is clearly observed, indicating a possible slight cargo shift to the front of the vessel. A second mechanism that could be responsible for the increased pitch of the vessel is the water level on top of the cargo indicated in Fig. 13. Snap shots of the bulk carrier during the simulation are displayed in Fig. 17, visualizing the interaction of the hull and the water surface. At $t = 25.0$ s and $t = 39.5$ s green water can be observed on deck of the vessel.

Overall, the feasibility study demonstrates the efficacy of a monolithic coupled 3D model in replicating the observed cargo behavior using a rigid perfectly-plastic material model. This methodology captures the mechanical behavior of materials that do not exhibit strain hardening or strain-rate sensitivity during yielding. However, the direct monolithic coupling of multi-physics processes with disparate time scales, encompassing cargo behavior on a vessel in waves, requires substantial computational resources. Expanding the approach to incorporate coupled seepage flow through rigid perfectly-plastic materials would further enhance the model's capabilities. This extension could account for the "wet base" and "dynamic separation" scenarios. However, such an expansion would also significantly increase computational costs.

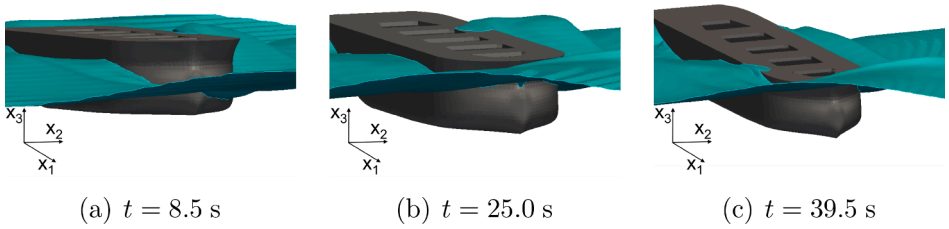

Fig. 17. Snap shots of bulk carrier in seaway during incident conditions as experienced by "Jian Fu Star".

6. Conclusion

We have presented and validated a monolithic numerical model for the transport of granular cargo on bulk carriers and applied the model to investigate a real accident scenario. This numerical framework provides a robust method to simulate the complex interplay between ship motion, wave dynamics and granular cargo behavior. Its application to the "Jian Fu Star" incident demonstrates its potential to improve maritime safety through a better understanding of bulk carrier stability and the related cargo shifting phenomena.

The validation and verification studies demonstrate the robustness and accuracy of the finite-volume based three-phase flow approach and the embedded granular material model. For the three-phase flow, the numerical results showed strong agreement with experimental data in terms of the temporal evolution of interfaces and the overall flow behavior. Although some discrepancies in the fracture behavior and velocity profiles were observed, likely due to different initial conditions, the model successfully captured the key dynamics of the dam break experiment. The granular model exhibited good agreement with PFEM results. The slight differences observed in wall adhesion stem from the different treatment of boundary interactions between the two methods.

The feasibility study on an actual accident involving a bulk carrier carrying nickel ore shows that cargo shifting occurred under the assumed weather and wave conditions, using the material properties and vessel and cargo dimensions given in the accident report. Results of the current feasibility study underscore the complex interplay between the vessel motion, the cargo behaviour and hold geometry in determining the spatial distribution and magnitude of cargo displacement during maritime transport. While the monolithic coupled 3D approach with rigid perfectly-plastic materials is promising in reproducing cargo behavior, the associated computational effort still represents a challenge for practical application. Future research should focus on balancing model fidelity with computational efficiency to make fully coupled 3D simulations more feasible for real-world applications.

Declaration of competing interest

The authors declare that they have no known competing financial interests or personal relationships that could have appeared to influence the work reported in this paper.

CRediT authorship contribution statement

W. Düsterhöft-Wriggers: Writing – original draft, Visualization, Validation, Software, Investigation, Formal analysis, Data curation; **T. Rung:** Writing – review & editing, Supervision, Project administration, Methodology, Conceptualization

Acknowledgments

The authors acknowledge the support within the research project "LiquefAction - Cargo Liquefaction in Ship Design and Operation" (Grant no. FKZ 03SX363A). Selected computations were performed with resources provided by the North-German Super-computing Alliance (HLRN).

Appendix A. Appendix

A.1. Vessel dimensions of "Jian Fu Star" model

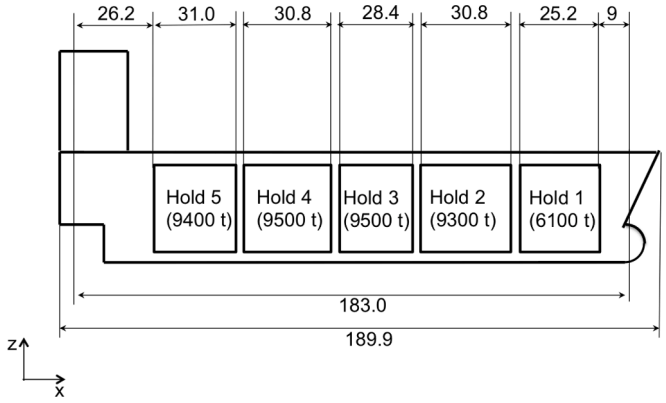

Fig. A.18. Arrangement of holds in bulk carrier "Jian Fu Star". Dimensions are given in meters.

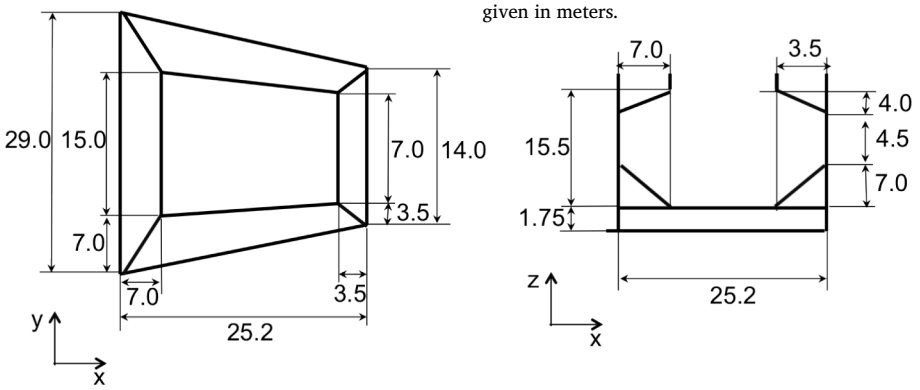

Fig. A.19. Geometry of hold one with dimensions given in metres.

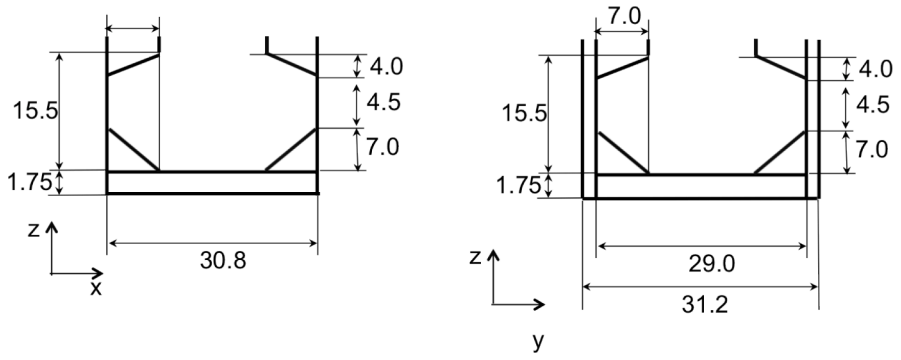

Fig. A.20. Geometry of hold two, hold three and hold four with dimensions given in metres.

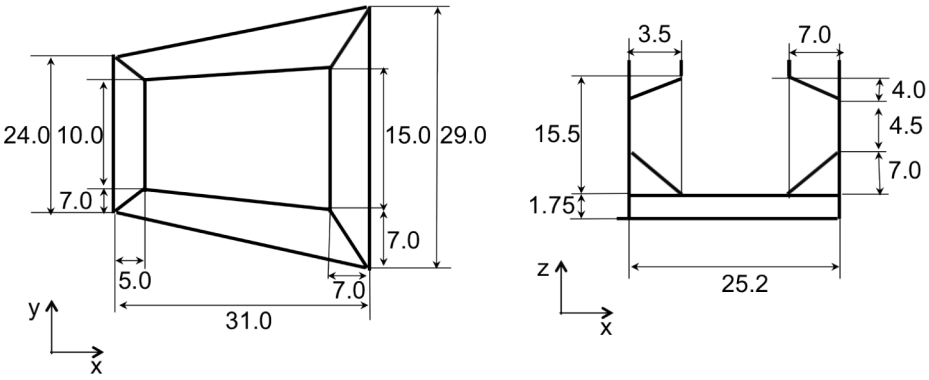

Fig. A.21. Geometry of hold five with dimensions given in metres.

References

Airey, D.W., Ghorbani, J., 2021. Analysis of unsaturated soil columns with application to bulk cargo liquefaction in ships. Comput. Geotech. 140, 104402.

Bian, H., Shahrour, I., 2009. Numerical model for unsaturated sandy soils under cyclic loading: application to liquefaction. Soil Dyn. Earthq. Eng. 29, 237–244.

Bui, H., Fukagawa, R., Sako, K., Ohne, S., 2008. Lagrangian meshfree particles method (SPH) for large deformation and failure flows of geomaterial using elastic-plastic soil constitutive model. Int. J. Numer. Anal. Methods Geomech. 32, 1537–1570.

Chupin, L., Dubois, T., 2024. Non-isochoric stable granular models taking into account fluidisation by pore gas pressure. J. Fluid Mech. 979, A14.

ClassNK, 2012. Guidelines for the Safe Carriage of Nickel Ore. Guidelines. Nippon Kaiji Kyokai.

Di, Y., Sato, T., 2004a. Computational modeling of large deformation of saturated soils using an ALE finite element method. Annu. Disas. Prev. Res. Ins 47, 171–182.

Di, Y., Sato, T., 2004b. A practical numerical method for large strain liquefaction analysis of saturated soils. Soil Dyn. Earthq. Eng. 24, 251–260.

Düsterhöft-Wriggers, W., Larese, A., Oñate, E., Rung, T., 2022. Assessment of simplified momentum equations for free surface flows through rigid porous media. Exp. Comput. Multiph. Flow. 5(2), 159–177.

Düsterhöft-Wriggers, W., Schubert, S., Rung, T., 2024. A two-phase volume of fluid approach to model rigid-perfectly plastic granular materials. Int. J. Numer. Methods Fluids 96 (12), 1813–1829. https://doi.org/10.1002/fld.5323

Elgamal, A., Yang, Z., Parra, E., 2002. Computational modeling of cyclic mobility and post-liquefaction site response. Soil Dyn. Earthq. Eng. 22, 259–271.

Ferauge, S., Jacobs, W., De Baere, K., 2019. "LIQUEFACTION" and "DYNAMIC SEPARATION" different aspects of the same problem. Int. J. Marit. Eng. 161 (A4).

Ferziger, J.H., Perć, M., 2008. Numerische Strömungsmechanik. Springer Verlag.

Gentaz, L., Luquet, R., Alessandrini, B., Ferrant, P., 2004. Numerical simulation of the 3D viscous flow around a vertical cylinder in non-linear waves using an explicit incident wave model. In: International Conference on Offshore Mechanics and Arctic Engineering. Vol. 37432, pp. 157–163.

Hasselmann, D.E., Dunckel, M., Ewing, J.A., 1980. Directional wave spectra observed during JONSWAP 1973. J. Phys. Oceanogr. 10 (8), 1264–1280. https://doi.org/10.1175/1520-0485(1980)010<1264:DWSODJ>2.0.CO;2

Hirt, C.W., Nicholls, B.D., 1981. Volume of fluid method for dynamics of free boundaries. J. Comput. Phys. 39, 201 – 221.

Hoang, T.N., Bui, H.H., Nguyen, T.T., Nguyen, T.V., Nguyen, G.D., 2024a. Development of free-field and compliant base SPH boundary conditions for large deformation seismic response analysis of geomechanics problems. Comput. Methods Appl. Mech. Eng. 432, 117370.

Hoang, T.N., Nguyen, T.T., Nguyen, T.V., Nguyen, G.D., Bui, H.H., 2024b. SPH simulation of earthquake-induced liquefaction and large deformation behaviour of granular materials using SANISAND constitutive model. Comput. Geotech. 174, 106617.

Investigation Department, M. A., 2011. REPORT: M/V "JIAN FU STAR" R-011-11-DIAM. Investigation report. Panama Maritime Authority.

Iron Ore Technical Working Group, 2013. Development of amendments to the IMSBC code and supplements, including evaluation of properties of solid bulk cargoes. The Technical Working Group (TWG) Report 4 "Reference Tests". DSC 18/INF.13. International Maritime Organization (IMO).

INTERCARGO, 2019. Bulk Carrier Casualty Report - Years 2009 to 2018 and Trends. Technical report. International Association of Dry Cargo Shipowners.

INTERCARGO, 2021. Bulk Carrier Casualty Report - Years 2012 to 2021 and Trends. Technical Report. International Association of Dry Cargo Shipowners.

Jacobsen, N.G., Fuhrman, D.R., Fredsoe, J., 2012. A wave generation toolbox for the open-source CFD library: openfoam. Int. J. Numer. Methods Fluids 70 (9), 1073–1088. https://doi.org/10.1002/fld.2726

Jánosi, I., Jan, D., Szabó, K., Tél, T., 2004. Turbulent drag reduction in dam-break flows. Exp. Fluids 37(2), 219–229.

Ju, L., Vassalos, D., Wang, Q., Liu, Y., 2019. Solid bulk cargo instability during marine transport. Ocean Eng. 186, 106089.

Ju, L., Vassalos, D., Wang, Q., Wang, Y., Liu, Y., 2018. Numerical investigation of solid bulk cargo liquefaction. Ocean Eng. 159, 333–347.

Kühl, N., Hinze, M., Rung, T., 2021. Cahn–Hilliard Navier–Stokes simulations for marine free-surface flows. Exp. Comput. Multiph. Flow. https://doi.org/10.1007/s42757-020-0101-3

Larese, A., 2012. A coupled eulerian-PFEM model for the simulation of overtopping in rockfill dams. Ph.D. thesis, International Center for Numerical Methods in Engineering.

Lee, H.L., 2017. Nickel ore bulk liquefaction a handymax incident and response. Ocean Eng. 139, 65–73.

Leonard, B.P., 1979. A stable and accurate convective modelling procedure based on quadratic upstream interpolation. Comput. Methods Appl. Mech. Eng. 19 (1), 59–98.

Luo, X., Rung, T., 2017. Computation of mechanically coupled bodies in a seaway. Ship Technol. Res. 64, 129–143. https://doi.org/10.1080/09377255.2017.1348654

Luo, X., Rung, T., 2019. Numerical analysis of the installation procedures of offshore structures. Ocean Eng. 179, 116–127. https://doi.org/10.1016/j.oceaneng.2019.03.004

Manzke, M., 2019. Development of a Scalable Method for the Efficient Simulation of Flows using Dynamic Goal-Oriented Local Grid-Adaptation. Ph.D. thesis. Hamburg University of Technology.

Munro, M.C., Mohajerani, A., 2016. Liquefaction incidents of mineral cargoes on board bulk carriers. Adv. Mater. Sci. Eng. 2016(1), 5219474.

Rhie, C.M., Chow, W.L., 1983. Numerical study of the turbulent flow past an airfoil with trailing edge separation. AIAA 21.
Rose, T. P., 2014. Solid Bulk Shipping: Cargo Shift, Liquefaction and the Transportable Moisture Limit.
Rung, T., Wöckner, K., Manzke, M., Brunswig, J., Ulrich, C., Stück, A., 2009. Challenges and perspectives for maritime CFD applications. Jahrb. Schiffbautech. Ges. 103, 127–39.
Teutsch, I., Groll, N.,. Seegangsbetrachtung zum untergang der MS MELANIE SCHULTE im Jahr 1952. Die Küste 93. https://doi.org/10.18171/1.093104
Ulrich, C., Leonardi, M., Rung, T., 2013. Multi-physics SPH simulation of complex marine-engineering hydrodynamic problems. Ocean Eng. 64, 109–121.
Unno, T., Kazama, M., Uzuoka, R., Sento, N., 2008. Liquefaction of unsaturated sand considering the pore air pressure and volume compressibility of the soil particle skeleton. Soils Found. 48, 87–99.
Völkner, S., Brunswig, J., Rung, T., 2017. Analysis of non-conservative interpolation techniques in overset grid finite-volume methods. Comput. Fluids 148, 39–55.
Wang, Z., Zhang, J., Zhou, H., 2022. Numerical study on the influence of angles of repose on the stability of cargo in a cargo hold. J. Phys. 2195, 012001. https://doi.org/10.1088/1742-6596/2195/1/012001
Wilcox, D.C., 2004. Turbulence Modeling for CFD. DCW Industries, Inc., second ed.
Wobbes, E., Beuth, L., Vuik, C., Stolle, D., 2017. Modeling of liquefaction using two-phase FEM with UBC3D-PLM model. Procedia Eng. 175, 349–356.
Wöckner, K., Drazyk, W., Rung, T., 2010. An efficient VOF-based RANS method to capture complex sea states. ASME 29th International Conference on Ocean, Offshore and Arctic Engineering (OMAE2010), Shanghai, China.
Wu, W., Li, Y., Zhao, Z., Zheng, Q., Zhang, C., Ji, H., Yu, X., Yu, S., 2022. Quantitative analysis of liquefaction risk of liquefiable solid bulk cargoes during sea transport. Ocean Eng. 258, 111751. https://doi.org/10.1016/j.oceaneng.2022.111751
Yakubov, S., Maquil, T., Rung, T., 2015. Experience using pressure-based CFD methods for Euler–Euler simulations of cavitating flows. Comput. Fluids 111, 91–104.
Zhang, J., Wu, W., Zhao, Z., Chen, Y., 2019. Numerical study on coupled effect of a vessel loaded with liquefied nickel ore. J. Mar. Sci. Technol. https://doi.org/10.1007/s00773-019-00658-9
Zou, Y., Shen, C., Xi, X., 2013. Numerical simulations on the capsizing of bulk carriers with nickel ores. J. Navig. 66, 919–930.